Research Square

Preprints are preliminary reports that have not undergone peer review.
They should not be considered conclusive, used to inform clinical practice,
or referenced by the media as validated information.

Self-regulated immune-neurovascular bone repair scaffold via functional surface features

Dongmei Yu
Air force medical university, tangdu hospital
Zhen Tang
Air force medical university, tangdu hospital
Tonglei Yang
Air force medical university, tangdu hospital
Shuo Guo
Air force medical university, tangdu hospital
Shusen Bao
Air force medical university, tangdu hospital
Chenyu Li
Air force medical university, tangdu hospital
Qi Wu
Air force medical university, tangdu hospital
Changchen Chen
Air force medical university, tangdu hospital
Yingxiang Liu
Air force medical university, tangdu hospital
Xiaokang Li
Air force medical university, tangdu hospital
Hai Huang
Air force medical university, tangdu hospital
Hao Wu
Air force medical university, tangdu hospital
Zheng Guo
guozheng@fmmu.edu.cn
Air force medical university, tangdu hospital

Research Article

Keywords: functional surface feature, self-regulated immunoreaction, angiogenesis and vascularization, neurogenesis and innervation, osteogenesis and osseointegration

Posted Date: July 28th, 2026

DOI: https://doi.org/10.21203/rs.3.rs-10012508/v1

License: This work is licensed under a Creative Commons Attribution 4.0 International License. Read Full License

Additional Declarations: No competing interests reported.

Version of Record: A version of this preprint was published at Advanced Composites and Hybrid Materials on September 26th, 2026. See the published version at https://doi.org/10.1007/s42114-026-02095-w.

Self-regulated immune-neurovascular bone repair scaffold via functional surface features

Dongmei Yu[a,b,1], Zhen Tang [c,a,1], Tonglei Yang [a, 1], Shuo Guo[d,e,1], Shusen Bao[a,f], Chenyu Li[a,], Qi Wu[a], Changchen Chen[a], Yingxiang Liu[a], Xiaokang Li[a], Hai Huang[a, *], Hao Wu[a,*], Zheng Guo [a,*]

[a] Department of Orthopedics, Tangdu Hospital, Air Force Medical University, Xi'an, 710038, China

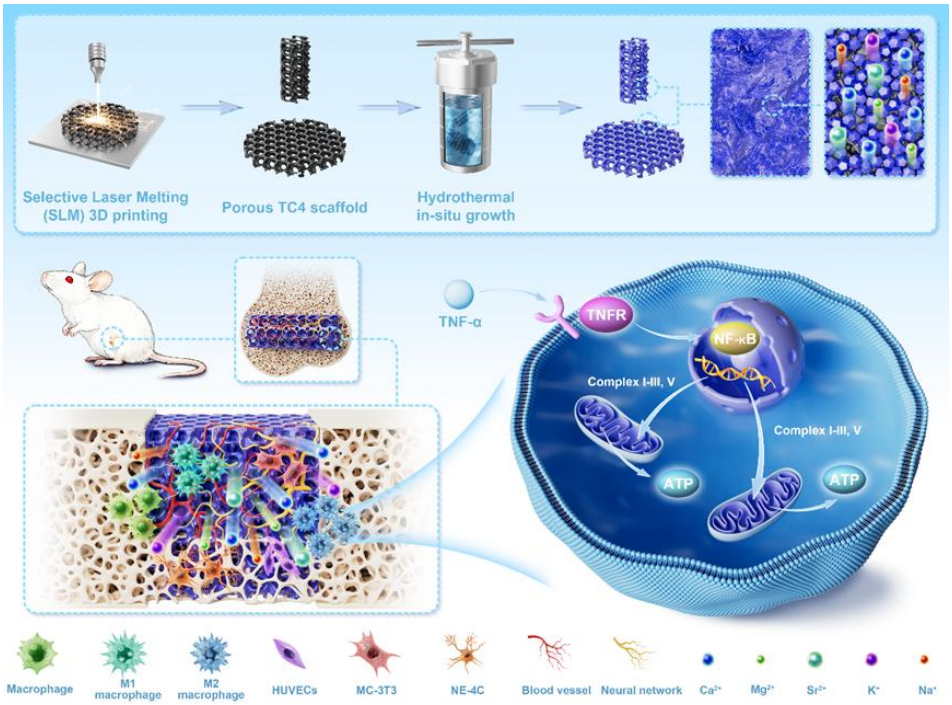
[b] Institute of Orthopaedic and Musculoskeletal Science, University College London, Royal National Orthopaedic Hospital, Stanmore, London HA7 4LP, UK

[c] Department of Orthopaedics, General Hospital of Central Theater Command (Wuhan General Hospital of Guangzhou Command, previously), Wuhan 430030, China

[d] Department of Biomedical Engineering, Air Force Medical University, Xi'an 710032, China

[e] Department of Radiology, Tangdu Hospital, Air Force Medical University, Xi'an 710038, China

[f] Department of Orthopedics, No. 903 Hospital of PLA Joint Logistic Support Force, Hangzhou, 310000, China



Graphic Abstract

Abstract: Given specific microenvironment of bone repair, the bio-functionally decorated implant endowed with self-regulated bone healing procedure was committed to pursuing. Inspired by the microstructure and chemical composition of natural bone, a kind of bionic bone-like bioactive

* Corresponding author: guozheng@fmmu.edu.cn. Tel.: +86 02984777433.
* Corresponding author: 15619421671@163.com.
* Corresponding author: haihuang_snow@126.com.
[1] Co-first authors: These authors contributed equally to this work.

coating, namely micro/nano gradient morphological calcium titanate containing trace ions, was in-situ hydrothermally grown on 3D printed porous titanium alloy scaffold. Surface features of the decorated porous titanium alloy scaffolds, by itself, could modulate microenvironment, and enhance neurovascular bone regeneration and reconstruction via surface topography and sustainably released bioactive ions, as verified by in vitro and in vivo biological evaluation. The underlying immunoregulation mechanism was surface feature-modulated macrophage oxidative phosphorylation and ATP production in energy metabolism, which advocates M2 macrophage phenotypic switch. It provided an insightful foundation for bio-functional decoration of bone repair implants.

Key words: functional surface feature, self-regulated immunoreaction, angiogenesis and vascularization, neurogenesis and innervation, osteogenesis and osseointegration

Introduction

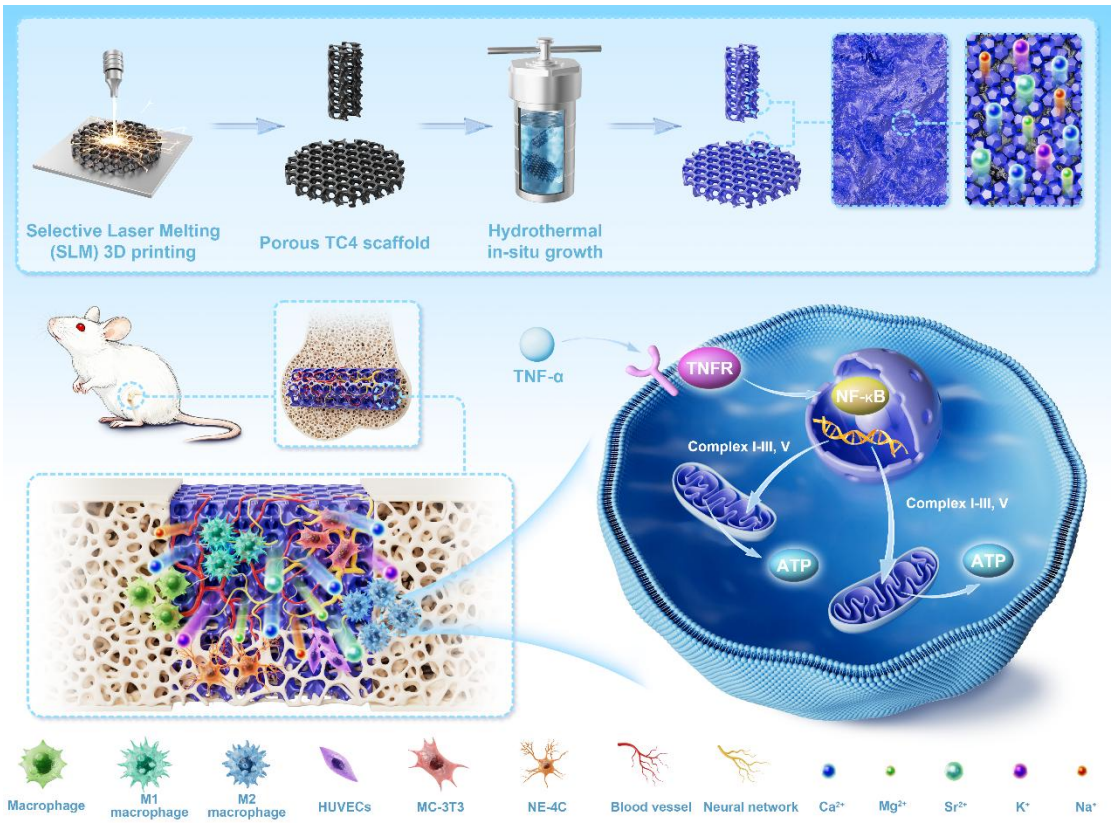
Personalized 3D printing technology was successfully applied to fabricate bone repair prostheses (*1, 2*). Titanium alloys due to their load-bearing capability and biocompatibility, are commonly used as orthopedic implants (*3*). However, inherent bio-inertness and internally inadequate bone in-growth on porous titanium alloy scaffolds of customized 3D printing in clinical application, hampered osseointegration efficiency and bone healing period (*4*). Therefore, functional surface modification, including biomimetic micro/nano gradient morphology and chemical composition of natural bone, was applied to improve osteogenic behavior of 3D printed titanium alloy porous scaffolds. Given inorganic composition of natural bone, a strategy for the incorporation of dominated calcium element and trace elements (such as sodium, magnesium, potassium and strontium) into functional surface coating in-situ grown on 3D printed titanium alloy scaffolds was preferred. Furthermore, functionally decorated implant surface can modulate biological function via physical and chemical properties (eg. morphology, composition and hydrophily) during bone reconstruction (*5, 6*). Current clinical strategies predominantly focus on biomaterial intelligently self-regulated bone repair process (*7, 8*). Surface functionalization of bioactive material scaffolds eventually determines their biological performance, with materials of varying functions exhibiting distinctly different osteogenic capabilities.

Bone tissue depends on the intricate interplay between blood vessels and nerve networks, both of which essentially operate and participate in many physiological and pathological processes of the

skeletal system. The skeleton is highly innervated by numerous blood vessel and nerve fibers widely distributed in the periosteum, bone marrow and Haversian system, which support various physiological activities in modulating bone regeneration and sensations via neurotransmitter secretion and blood transportation bone (*9, 10*). On one hand, blood vessels invaded into ossification center provide the necessary nutrients and oxygen to nerves and bone while aiding in the removal of waste metabolic product (*11*). In addition, proangiogenic factors and angiogenic molecules facilitate neurogenesis and axon patterning. On the other hand, nerve cells can modulate blood vessel function and command blood flow via neurovascular coupling in bone, and besides neural crest contributes to the vascular system formation. Osseointegration process during bone defect repair is involved in the crosstalk of various cell types and tissue through intricate signaling networks, where immune cells closely interact with neuro-vascular cells to function bone defect repair in response to implanted materials (*12*). In fact, all the kinds of cells, especially macrophages, are responsive to functional decoration, upon adhering to implant surface. Neurovascular-bone tissue engineering emphasizes facilitating neurovascular innervation, and synergistic regeneration and ingrowth of nerves, blood vessels and bones (*13*). The scaffolds mimicking surface microstructure and inorganic composition of natural bone, have been endowed with the capability to regulate cell behavior, realize the immunomodulation of bone regeneration and support the ingrowth of nerves and blood vessels. Bioactive metal ions were applied to boost bone regeneration and bone fracture healing via the enhancement of vascular growth, osteogenic activity. For example, magnesium, calcium and strontium ions could promote angiogenesis and osteogenesis (*14, 15*). Ca^{2+} was validated to regulate the proliferation, migration, and differentiation of neural stem cells (*16, 17*). Moreover, the released Mg^{2+} ions contributed to nerve and blood vessel formation (*18*). Bioactive ion incorporation is conductive to vascular bone healing.

Inspired by bone mineral containing ions, cubic multi-ions-doped Na_2TiO_3 nanorod-like coatings for immunomodulatory promotion on vascularized bone apposition were validated, suggesting that calcium ions dominated the acceleration efficiency in assist with the ions of trace elements in bone (*19*). As previous another research done, micro/nano-topographic $CaTiO_3$ coating, especially 10%H_2O_2-Ca, driven immunoregulatory neuro-vascularized osseointegration was verified and its underlying mechanism was attributed to signaling pathway of CaSR→PI3K→AKT (*20*). It indicated that surface features of the decorated porous scaffolds modulated oxidative

phosphorylation in energy metabolism. Furthermore, bioactive ions contributed to vascularized bone repair via immune response, while their effect on neural differentiation in bone regeneration has been unknown. On basis of previous research, bioactive ions were furthermore incorporated into optimized micro/nano-topographic $CaTiO_3$ coating on 3D printed porous scaffolds. Herein, gradient micro/nanostructured multi-ion doped $CaTiO_3$ coating on 3D printed porous titanium alloy scaffold was prepared via in-situ hydrothermal growth, and then its neurogenesis-angiogenesis coupling driven osteoimmunology in vitro and in vivo was evaluated to explore the underlying mechanism (Scheme 1). Bridging immune-neurovascular crosstalk via the immunomodulatory surface feature of implanted scaffold for facilitating bone repair was worthy exploring.



Scheme 1. Schematic diagram of self-regulated immune-neurovascular bone repair modulated by micro/nanostructured multi-ion doped $CaTiO_3$ coating

Results and discussion

Structural characterization

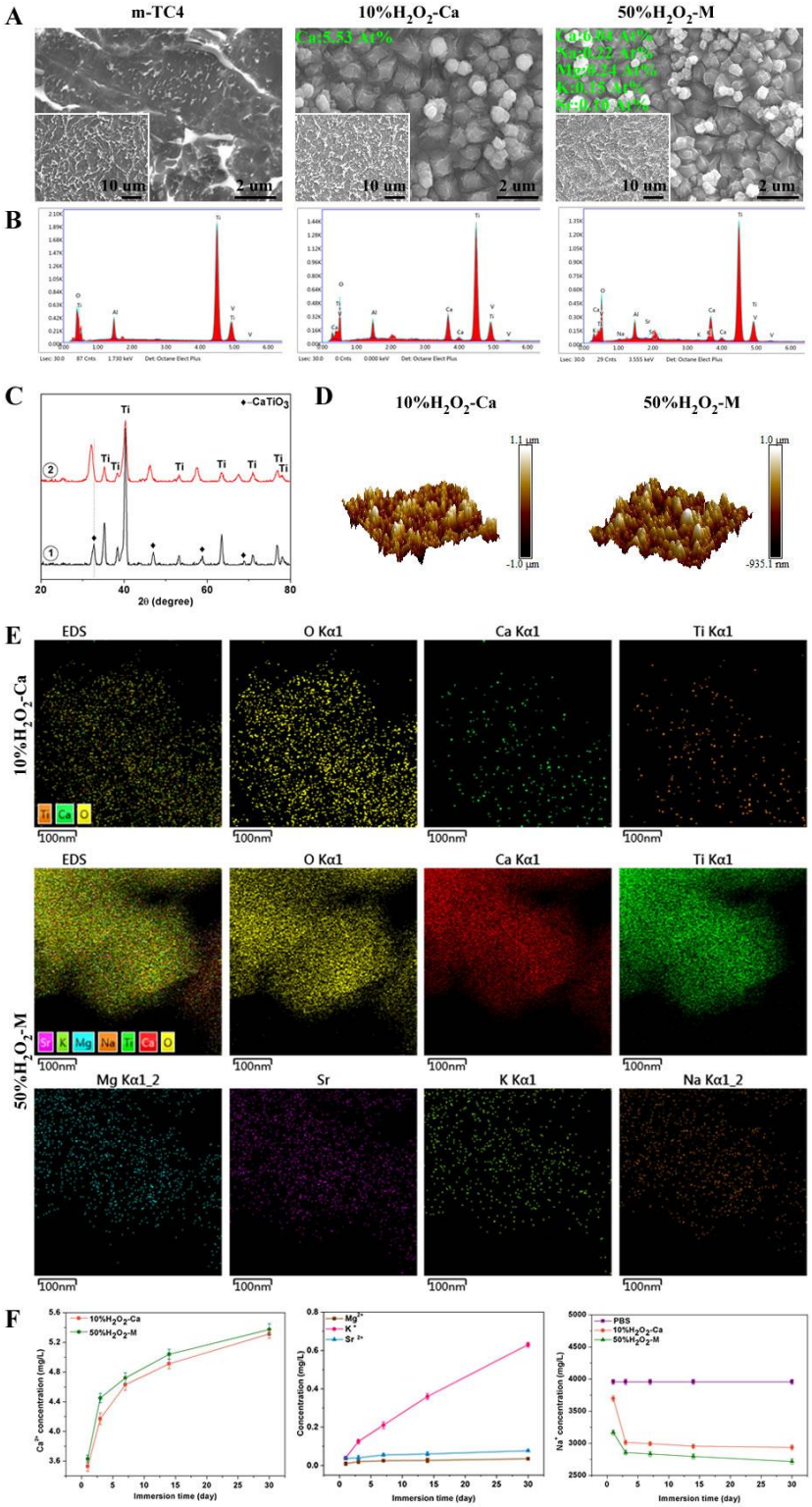


Fig. 1 (A) High magnified SEM images (bottom left illustration showing low magnified SEM images), and (B) SEM-mode EDS spectra of m-TC4, 10% H_2O_2-Ca and 50% H_2O_2-M coatings on porous titanium alloy scaffolds. (C) Thin-film XRD patterns and (D) surface nano-roughness images, TEM-mode EDS mapping images of nanostructures scrapped from 10% H_2O_2-Ca and 50% H_2O_2-M scaffolds, and (F) ion release profiles of 10% H_2O_2-Ca (Ca^{2+}) and 50% H_2O_2-M (Ca^{2+}, Mg^{2+}, K^+ and Sr^{2+}) coatings with immersion time, together with Na concentration variation of primitive and scaffold-immersed PBS (K^+-free) solutions at different immersion time.

Low magnified SEM images revealed that micro-scaled groove pits emerged on acid-etched scaffolds, while high magnified m-TC4 displayed locally amplified acid-etched texture and similar nano-morphological granules generated on 10% H_2O_2-Ca and 50% H_2O_2-M scaffolds (Fig. 1A). EDS spectra on nano-topological appearance, compared with m-TC4, uncovered that Ca element was comprised in 10% H_2O_2-Ca and Ca, Na, Mg, K and Sr were contained in 50% H_2O_2-M (Fig. 1B). Additionally, the cation contents at weight percent inserting into high magnified SEM images were semi-quantitatively detected by SEM-equipped EDS spectrum (Fig. 1A). XRD patterns indicated that characteristic peaks of calcium titanate ($CaTiO_3$) existed on 10%H_2O_2-Ca scaffold surface, while no new characteristic peaks emerged on 50% H_2O_2-M scaffold surface, excluding slight shift in characteristic peaks of $CaTiO_3$ (Fig. 1C). Nano-scaled roughness photographs showed that 10%H_2O_2-Ca and 50% H_2O_2-M scaffold surfaces displayed similar nano-scaled roughness values (Fig. 1D) regardless of the difference in chemical composition (Fig. 1A). EDS mapping images under TEM mode demonstrated element compositions and distributions on both scaffolds, in accordance with the results of SEM-mode EDS spectra (Fig. 1E). Ca ion release profiles of 10%H_2O_2-Ca and 50% H_2O_2-M scaffolds disclosed slightly rapid release, and Mg, K and Sr ions released from 50% H_2O_2-M scaffold via exchanging with Na ions in PBS solution as immersion time prolonged (Fig. 1F). It attributed to the stability of cubic-structured lattice in multi-ions incorporated $CaTiO_3$, which could not degrade but release doped ions via exchanging with Na ions in PBS solution (*19*). Totally, mirco/nanostructured multi-ion doped calcium titanate coating was hydrothermally grown on 3D printed titanium alloy scaffold, and bioactive ions could slowly release from above-mentioned bioactive coating.

It noted that bioactive ions could modulate cell activity, such as inflammation response, angiogenic and osteogenic behavior, and following bone reconstruction. X-ray photoelectron spectroscopy (XPS) for full spectra and high-resolution spectra of Ca 2p, O 1s and Ti 2p on 10% H_2O_2-Ca scaffold further demonstrated the formation of Ca-O and Ti-O bonds, corresponding to $CaTiO_3$ (Fig. 2A). High-resolution spectrum of Ca 2p at 346.0 and 349.6 eV uncovered $CaTiO_3$ intense peak deriving from alkaline thermal reaction between $CaCl_2$ solution and titanium alloy substrate under strong oxidizing conditions (*21*). High-resolution spectrum of O1s exhibited a peak at 529.2 eV stemming from Ca-O and Ti-O bonds in $CaTiO_3$, while Ti 2p at 458.0, 463.8 and 471.5 eV were deemed to originate from $CaTiO_3$ (*22*). Sr 3d intense peaks at 133.0 and 135.1 eV were

attributed to $SrTiO_3$, while Mg 1s intense peaks at 1302.6 and 1304.9 eV were considered to be $MgTiO_3$ (*23, 24*). Na 1s intense peaks at 1068.4, 1073.2 and 1075.0 eV were deemed as Na_2TiO_3 (*25, 26*). K 2p intense peaks at 288.4 and 303.2 eV were taken for K_2TiO_3 (*27*). Hence, XPS high-resolution spectra of additional K 2p, Na 1s, Mg 1s and Sr 3d, besides Ca 2p, O 1s and Ti 2p, on 50% H_2O_2-M scaffold, revealed that K, Na, Mg, Sr ions were incorporated into $CaTiO_3$ lattice and combined with O ions to form ionic bonds, with bond energy consistent in those of respective titanate. It attributed to enough energy during above-mentioned titanate formation supplied by strong alkaline solution in strongly oxidizing hydrogen peroxide, along with high temperature. Collectively, XPS full spectra and high-resolution spectra further demonstrated the formation of multi-ion doped calcium titanate coating.

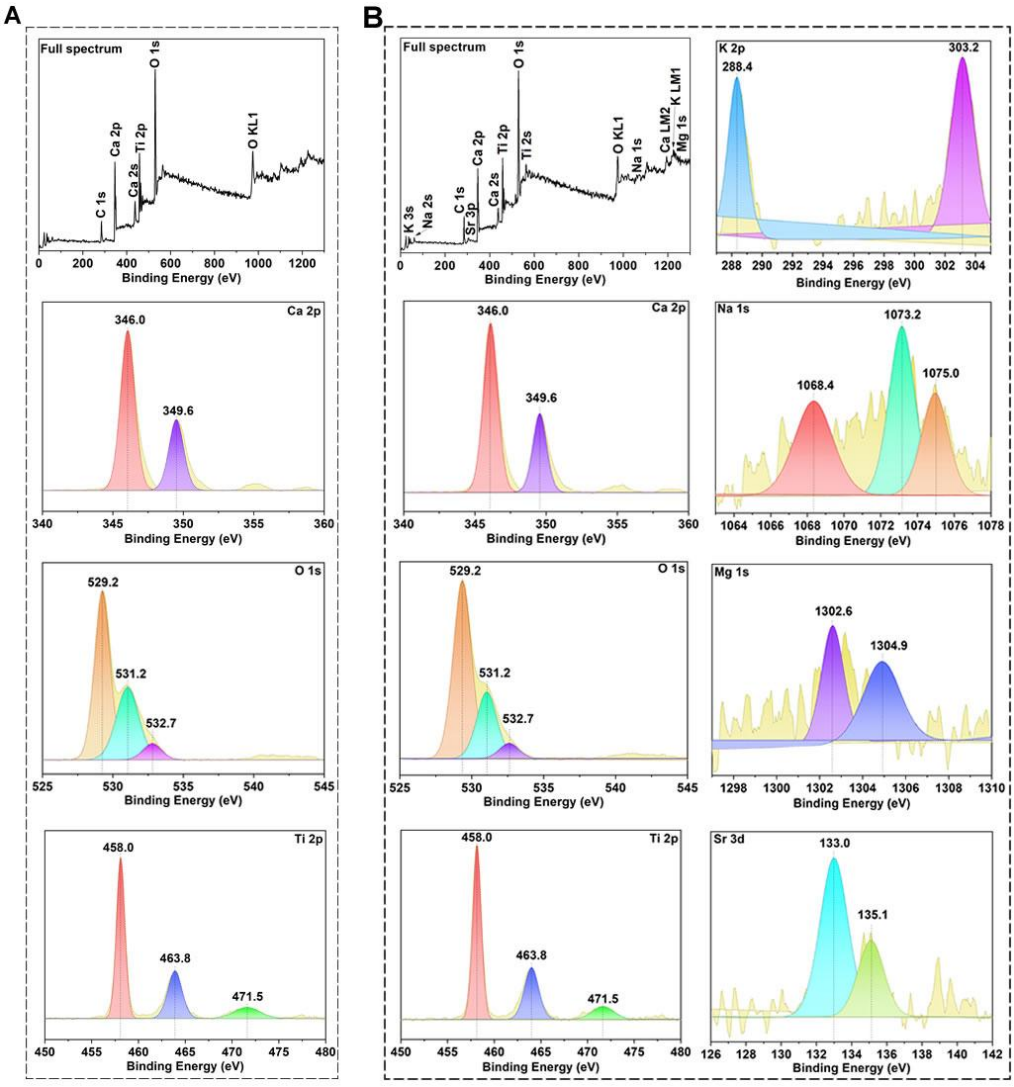


Fig. 2 XPS full spectra and high-resolution spectra of Ca, O, Ti, K, Na, Mg and Sr on (A) 10% H_2O_2-Ca and (B) 50% H_2O_2-M coated porous titanium alloy scaffolds, respectively.

Regulation of immune response

Polarization behavior of macrophages seeded on m-TC4, 10%H_2O_2-Ca and 50%H_2O_2-M scaffolds for 3 days was identified by fluorescence staining and cytokines section of inflammation related markers. Fluorescence staining images of green-staining iNOS (M1 marker, pro-inflammation), red-staining CD206 (M1 marker, pro-inflammation) and blue-staining nuclei in polarized macrophages and their quantified analysis, displayed pro-inflammatory reaction on m-TC4, but anti-inflammatory reaction on 10%H_2O_2-Ca and 50%H_2O_2-M with more significant effect. Section levels of pro-inflammatory TNF-α, and anti-inflammatory IL-10 cytokines displayed the results in accordance with those of fluorescence staining. Furthermore, the secretion of pro-angiogenic VEGF and PDGF-BB, as well as pro-neural NGF and pro-osteogenic BMP2 cytokines contributed to profitable micro-environment for angiogenesis and osteogenesis via immunomodulation. TNF-α encouraged osteoclast maturation beyond osteogenic function (*28*). IL-10 exerts as a M2-stated macrophage secreted protein with crucial immune regulatory and direct pro-osteogenic functions (*29*). VEGF is a chemotactic agent in the induction of vascular permeability, endothelial cell migration and proliferation, thereby facilitating angiogenesis (*30*). Platelet-derived growth factor-BB (PDGF-BB), mediated the formation of H-typed ($CD31^{high}EMCN^{high}$) vessels and eventually induced angiogenic–osteogenic coupling (*31, 32*). NGF is fundamental for osteocyte differentiation and mineralization, as it is prominently upregulated acutely following bone injury and its absence impairs fracture healing (*33*). BMP2 is capability of not only boosting osteogenesis but also playing an immunoregulatory role in osteogenic cascade (*34*). In summary, functionally decorated scaffolds, especially 50%H_2O_2-M, contribute to modulating macrophages to polarize into M2 phenotype and secreting inflammation- and osteogenesis-related cytokines, exhibiting anti-inflammatory response for favorable healing promotion.

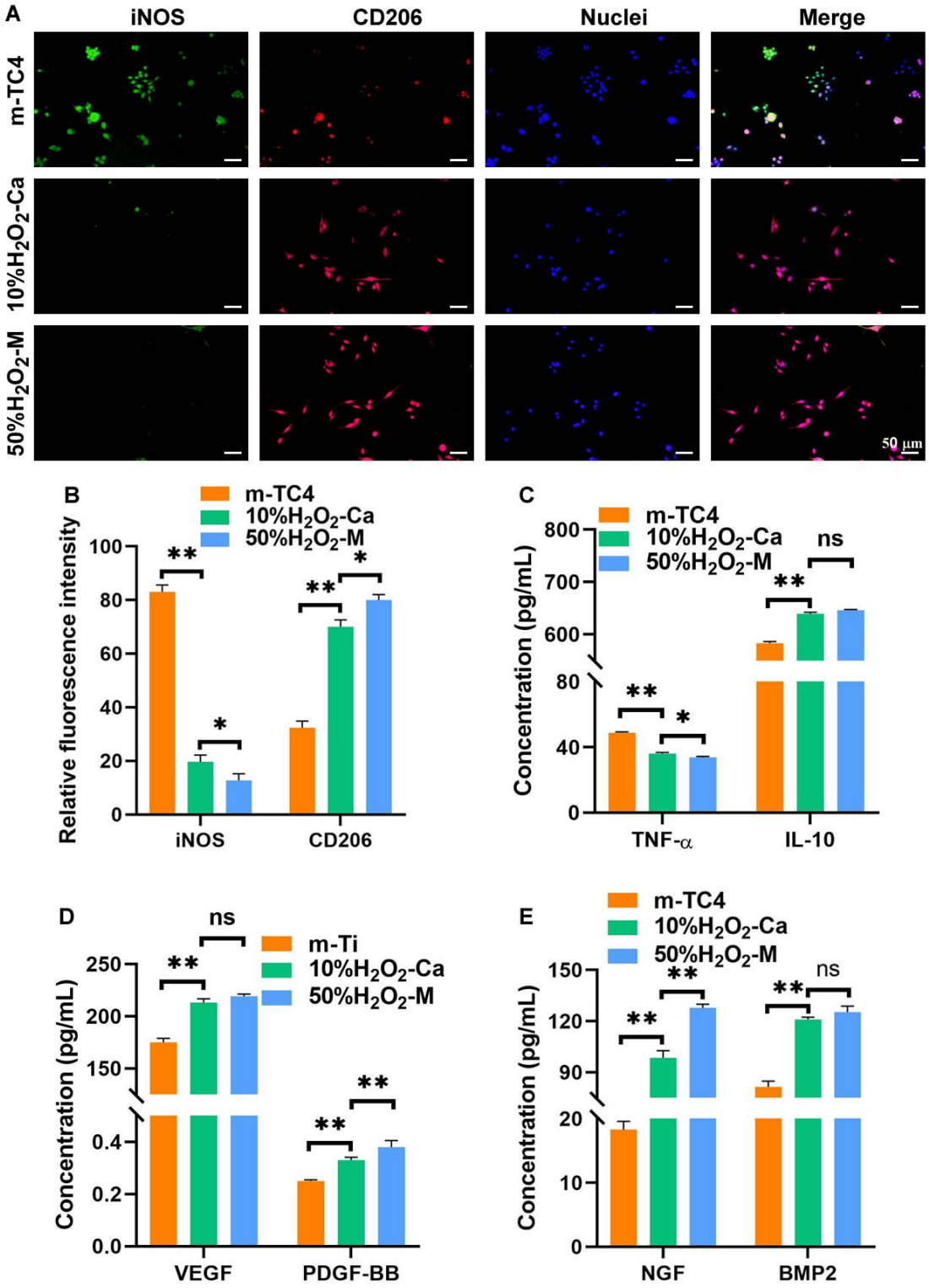


Fig. 3 Phenotypic polarization of macrophages incubated on m-TC4, 10%H_2O_2-Ca and 50%H_2O_2-M at day of 3: (A) fluorescence images of iNOS (green), CD206 (red) and nuclei (blue) in RAW264.7 cells along with (B) iNOS and CD206 relative fluorescence intensity. The cytokine concentration of (C) inflammation-related TNF-α and IL-10, (D) pro-angiogenic VEGF and PDGF-BB, (E) NGF and BMP2 secreted by macrophages on above-mentioned scaffolds. *: $p < 0.05$, **: $p < 0.01$.

Immunoregulatory angiogenesis

Crystal violet staining visualized the invaded HUVECs in response to the cytokine secretions of adhered macrophages on scaffolds, and statistics analysis quantified the number of invaded cells. Compared with the stimulus of macrophages on m-TC4 scaffold, HUVECs in response to macrophages on 10%H_2O_2-Ca and 50%H_2O_2-M obviously exhibited strong cell invasion capability, while the counterparts stimulated by macrophages on 50%H_2O_2-M displayed more significant invasion efficiency, attributing to micro/nano morphology and bioactive ions (Fig. 4A, D). Capillary tubule formation images together with quantitative statistics for number of branch points per field and total capillary tube length, revealed less capillary network for m-TC4 group, but much more abundant capillary network for 50%H_2O_2-M than that for 10%H_2O_2-Ca group (Fig. 4B, E, F). Migration images of HUVECs at 0 and 24 h along with quantified migration distance percent, exhibited obvious migration capability for 50%H_2O_2-M and 10%H_2O_2-Ca groups compared with m-TC4 scaffold, especially 50%H_2O_2-M counterpart (Fig. 4C, G). Collectively, cell invasion visualized by crystal violet staining, capillary tubule formation and cell migration, consistently confirmed potently immunoregulatory angiogenesis of 50%H_2O_2-M and 10%H_2O_2-Ca scaffolds (especially the former) in comparison with m-TC4 group. It indicated that mirco/nano gradient topography along with bioactive ions (50%H_2O_2-M), compared with sole mirco/nano gradient topography (10%H_2O_2-Ca), synergistically promoted angiogenesis of HUVECs via immunoregulation of macrophages adhered on above-mentioned scaffolds.

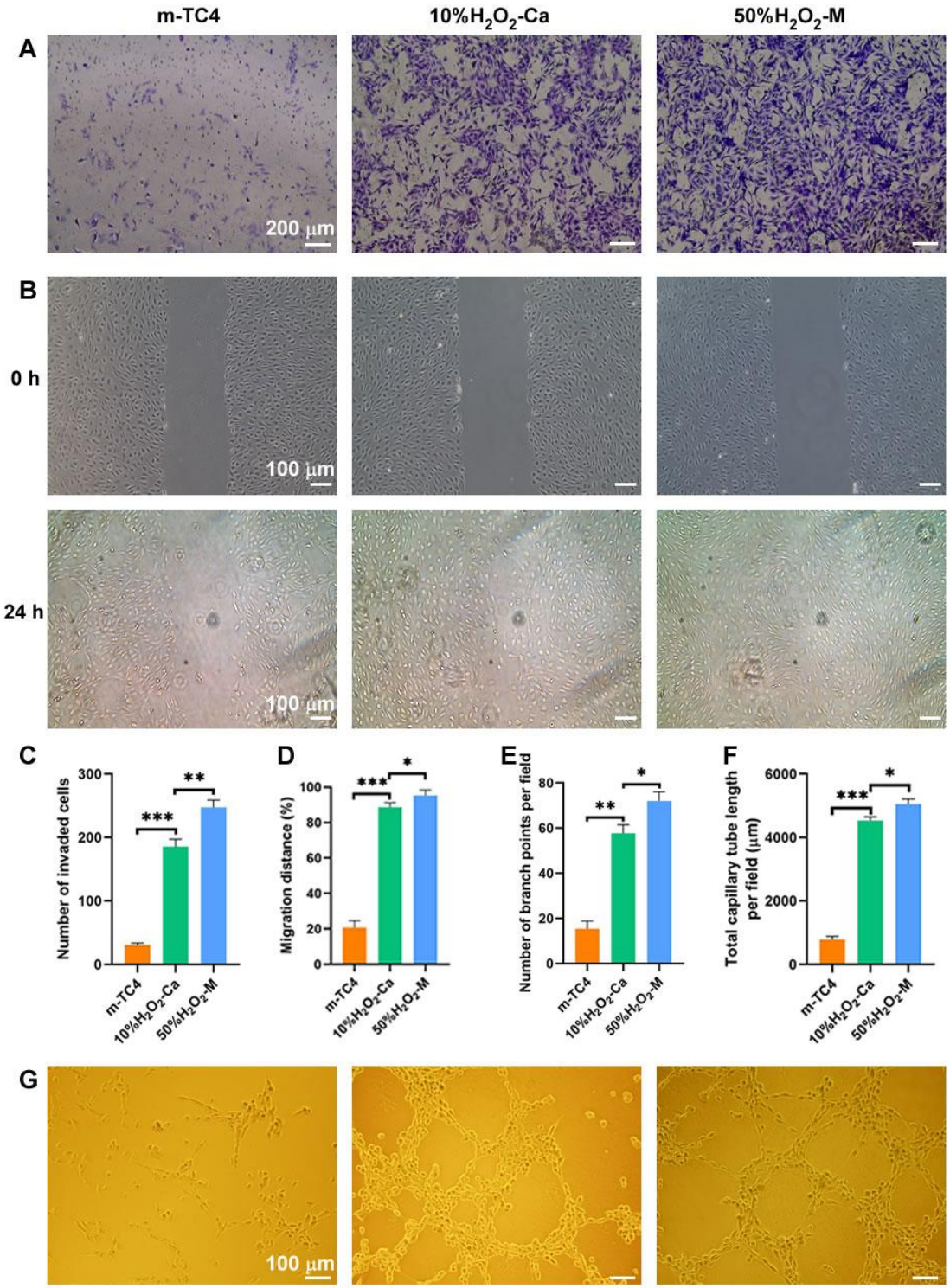


Fig. 4 Angiogenic capacity of HUVECs respectively stimulated by conditioned media from macrophages on m-TC4, 10%H_2O_2-Ca and 50%H_2O_2-M scaffolds for 3 days. (A, C) Representative crystal violet staining images of invasion assay and quantitation of invaded cell. (B, D) Migration images of HUVECs at 0 and 24 h, along with quantified migration distance percent. (G, E-F) Capillary tubule formation images, as well as their statistical analysis for number of branch points per field and total capillary tube length. *: $p < 0.05$, **: $p < 0.01$.

Immunoregulatory neurogenesis

Neural differentiation was characterized by fluorescence immunostaining of Nestin as an early neural marker, and MAP2 as a late neural marker in NE-4C cells, while the expression level of Nestin, an intermediate filament protein, commonly decreased once a neural network generated from differentiated cells (*35*). Herein, neural differentiation in NE-4C cells were stimulated by macrophages on m-TC4, 10%H_2O_2-Ca and 50%H_2O_2-M scaffolds and their secreted cytokines. Nestin and MAP2 highly expressed in NE-4C cells in response to macrophages on 10%H_2O_2-Ca compared with m-TC4 scaffolds, and their expression levels were highly significant for 50%H_2O_2-M group, as verified by fluorescence staining along with quantitatively relative fluorescence intensity (Fig. 5 A-C). Furthermore, NE-4C cells secreted pro-osteogenic cytokines of TGF-β and BMP2 to different degree in response to macrophages on above-mentioned scaffolds. Collectively, coated scaffolds, especially 50%H_2O_2-M, enhanced immunoregulatory neural differentiation of NE-4C cells in favor of the following neurogenesis via modulating phenotypic polarization of macrophages on scaffolds, attributing to micro/nano topography as well as slow release of bioactive ions.

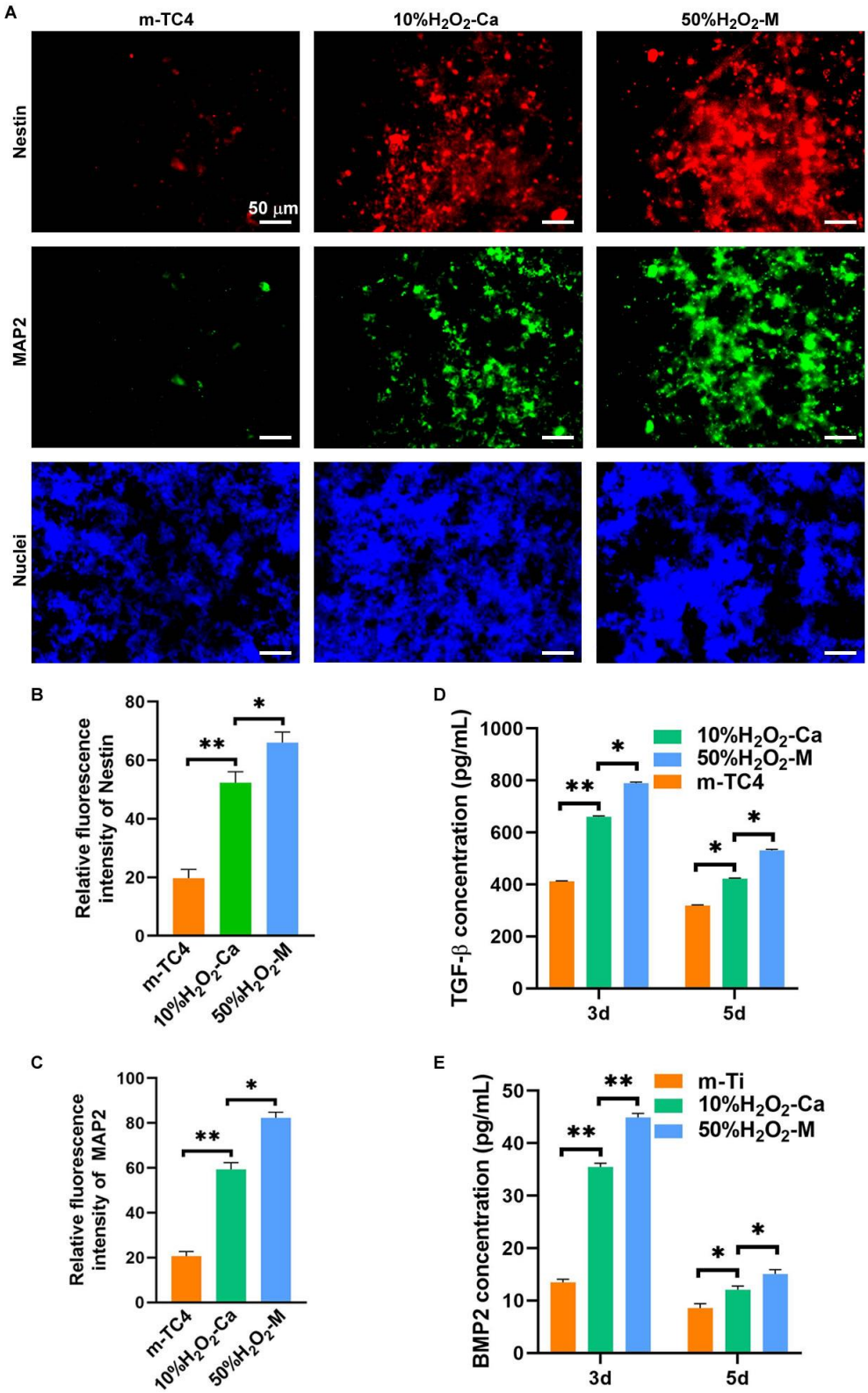


Fig. 5 Neural differentiation in NE-4C cells in response to macrophages on m-TC4, 10%H_2O_2-Ca and 50%H_2O_2-M scaffolds for 3 days. (A) Fluorescence staining images of Nestin (red), MAP2 (green) and nuclei (blue) in NE-4C cells, along with statistically relative fluorescence intensity of (B) Nestin and (C) MAP2. *: $p < 0.05$, **: $p < 0.01$.

Immunoregulatory osteogenesis

It is well known that osteogenesis was characterized by osteogenic differentiation and mineralization. ALP staining at 7 d and ARS at 14 d together with their respectively quantitative statistics uncovered that MC3T3-E1 cells in response to 3-day conditioned medium from macrophages on coated scaffolds, especially 50%H_2O_2-M, exhibited strong staining intensity representing high osteogenic differentiation and mineralization capability (Fig. 6). It indicated that coated scaffolds switched macrophage phenotype to pro-healing M2 state, and further regulated micro-environment to facilitate osteogenic differentiation and mineralization of MC3T3-E1 cells, profiting from surface gradient micro/nano morphology and slowly released bioactive ions on above-mentioned scaffolds. It was verified that both surface topography and bioactive ions contribute to obvious acceleration of bone growth. In summary, coated scaffolds accelerated immunoregulatory osteogenesis of MC3T3-E1 cells, with the most prominent efficiency for 50%H_2O_2-M counterpart.

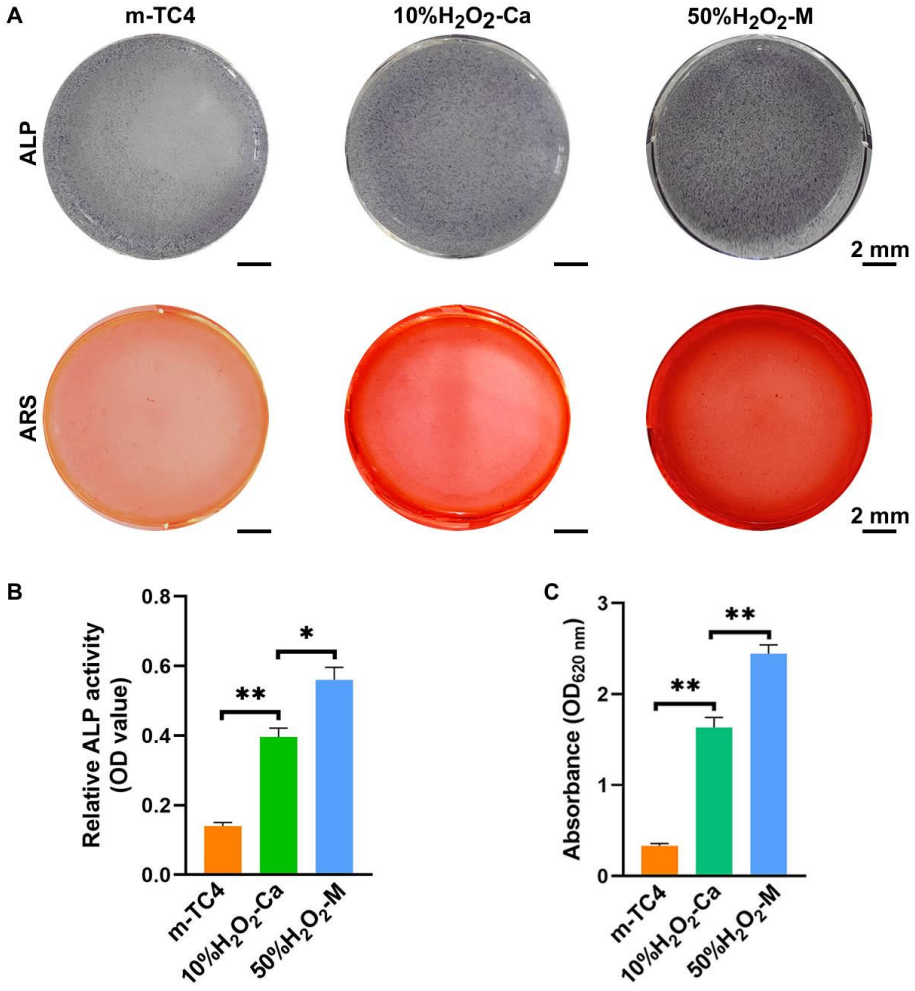


Fig. 6 Staining visualized osteogenesis of MC3T3-E1 cells in response to 3-day conditioned

medium from macrophages on m-TC4, 10%H_2O_2-Ca and 50%H_2O_2-M scaffolds. Photographs of (a) ALP staining at 7 d and ARS at 14 d respectively representing osteogenic differentiation and mineralization, and (B) their corresponding quantitative analysis. *: $p < 0.05$, **: $p < 0.01$.

The comparison between mono-culture of HUVECs/rBMSCs in response to ions released from the coatings, and co-culture of HUVECs/rBMSCs with MΦs on the coated and bare Ti discs, indicated the angiogenic and osteogenic capacity in co-culture case superior to mono-culture counterpart [19]. Given previous research, co-culture manner of HUVECs/NE-4C/MC3T3-E1 in response to macrophages on m-TC4, 10%H_2O_2-Ca and 50%H_2O_2-M scaffolds was directly applied to evaluate immune-neurovascular osseointegration. As known of Ca as primary element in natural bone, dominantly osteogenic function of calcium ion relative to other bioactive ions (such as Sr^{2+} and Mg^{2+}) was verified in previous research [19]. Herein, calcium titanate coating incorporated with some trace elements was establish to imitate the chemical composition of natural bone, and the synergistic effects of coating morphology and the sustained release of multiple bioactive ions were evaluated. Furthermore, the solo morphology effect of nano-topographied calcium titanate coating on immune-neurovascular osseointegration was validated [19]. Collectively, co-culture model and synergistic effects of coating morphology and the sustained release of multiple bioactive ions were meanwhile designed in this research.

RNA-sequence analysis and western verification of coated scaffold against inflammatory response

It was provisionally deduced that 50%H_2O_2-M scaffold was decorated with surface gradient micro/nano morphology and slowly released bioactive ions, which synergistically achieved self-regulated immune-neurovascular osseointegration. To uncover this underlying biological mechanism, RNA-sequence of macrophages adhered on TC4 and 50%H_2O_2-M scaffolds was identified to determine gene differences in transcript levels. The clustering heatmap and volcano plot of their differential gene expression revealed that the up-regulated genes were closely related to M2 phenotypic macrophages, while the down-regulated genes were associated with M1 phenotypic counterparts (Fig. 7A, B). Gene ontology (GO) disclosed that the effect of 50%H_2O_2-M scaffold on the biological processes, cellular components, and molecular functions of macrophages mainly focused on protein binding, signal transduction, and nuclear gene transcription, indicating that 50%H_2O_2-M scaffold switched macrophage polarization phenotype via facilitating cell

adhesion and subsequent nuclear transcription. Furthermore, analysis of the top 20 enriched pathways using Kyoto Encyclopedia of Genes and Genomes (KEGG) data revealed that immunoregulation-related pathways, including and signaling pathway, were highly enriched (Fig. 7C-E). These functional annotations suggested that 50%H_2O_2-M scaffold expedited macrophage polarization toward M2 phenotype due to the suppression of oxidative phosphorylation signaling axis.

In addition, representative protein expressions of in macrophages on 50%H_2O_2-M compared to that in macrophages on m-TC4 were detected. To verify the role of oxidative phosphorylation signaling axis in macrophage polarization mediated by synergetic assistance of surface micro/nano gradient morphology and released bioactive ions, TNF-α, Complex I, Complex II, and Complex IV protein levels in RAW264.7 cells on 50%H_2O_2-M vs m-TC4 scaffolds were visualized by western blotting and quantitative analysis of their gray values were conducted. It revealed that 50%H_2O_2-M stimulated macrophages expressed high levels in Complex I, Complex II, and Complex IV protein, but low level in TNF-α protein compared with m-TC4 stimulated macrophages. TNF-α, a central proinflammatory factor released in early inflammatory response, propelled the following involvement in inflammatory signaling procedure (*30*). It indicated that 50%H_2O_2-M scaffolds boosted macrophage phenotype switch from pro-inflammatory (M1) to anti-inflammatory (M2) phenotypes, probably attributing to their both surface micro/nano gradient morphology and released bioactive ions. Surface features on 50%H_2O_2-M scaffold influenced TNF-α protein, which regulated NF-$_k$B and further macrophage oxidative phosphorylation along with ATP production in energy metabolism, and thus advocated M2 macrophage phenotypic switch. It achieved implant surface feature-modulated immune-neurovascular bone repair, highlighting self-regulated characteristic of customized functional implant.

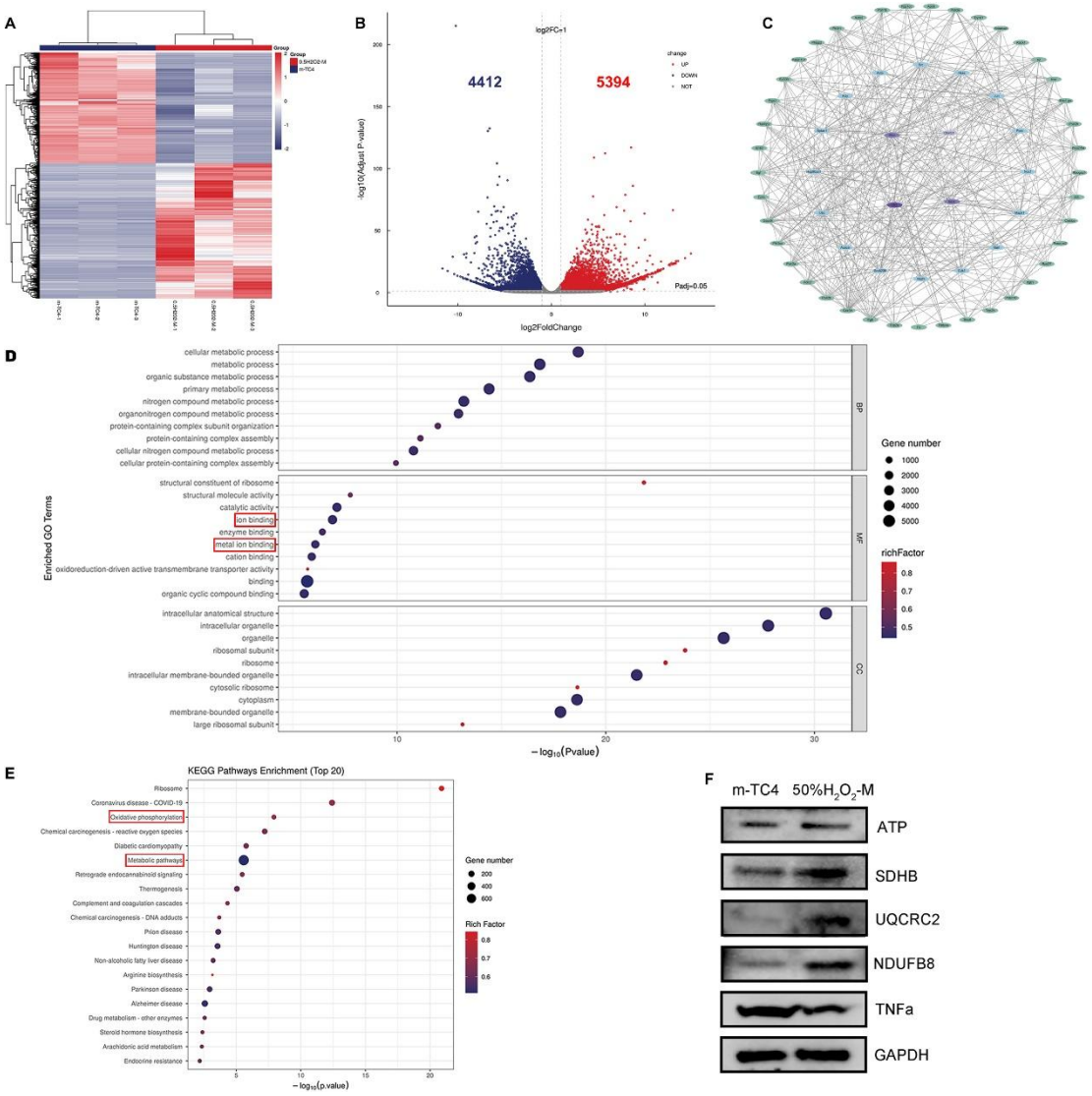


Fig. 7 RNA- sequence analysis and western verification of differentially expressed genes in macrophages on 50%H_2O_2-M versus on m-TC4 scaffolds. (A) Heatmap diagram, (B) volcano plot, (C) protein interaction network analysis, (D) Gene Oncology (GO) pathway enrichment, (E) Kyoto Encyclopedia of Genes and Genomes (KEGG) pathway enrichment analyses and (F) representative western blots of inflammation-associated signaling pathways.

***In vivo* immune-neurovascular osseointegration**

To visualize angiogenesis and vascularization within and around m-TC4, 10%H_2O_2-Ca and 50%H_2O_2-M scaffolds at 2 w post-surgery, neovascular network perfused with fluorescent agent was reestablished on basis of micro-CT scanning data. The images of capillary tube reconstruction with and without scaffold, as well as capillary tube distribution and diameter were showed (Fig. 8A), and capillary tube volume, surface and diameter were statistically quantified (Fig. 8B-D). It revealed that sparse neovascular network emerged within and around m-TC4 scaffold, while abundant neovascular network appeared within and around 10%H_2O_2-Ca scaffold, and more abundant neovascular network within and around 50%H_2O_2-M scaffold. Furthermore, new capillary tube with high volume, area and diameter were regenerated within and around 10%H_2O_2-Ca scaffold compared with m-TC4 counterpart, while more obvious efficiency within and around 50%H_2O_2-M. It indicated that coated scaffolds, especially 50%H_2O_2-M, enhanced significant neovascularization, attributing to synergistic action of micro/nano gradient morphology and sustainedly released multi bioactive ions, rather than sole effect of micro/nano gradient morphology for 10%H_2O_2-Ca scaffold.

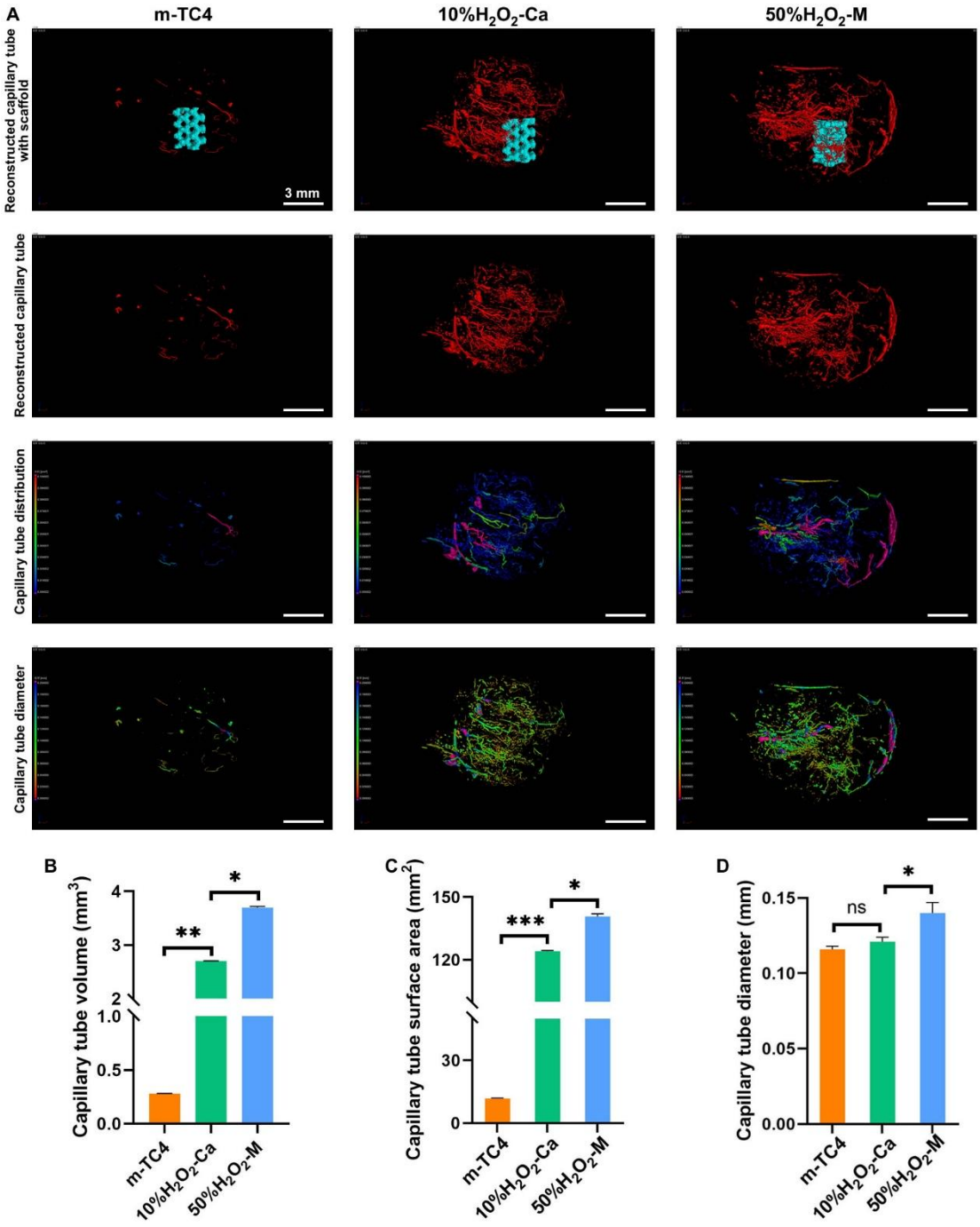


Fig. 8 Neovascular network within and around scaffolds at 2 w post-surgery visualized by fluorescent agent perfused through blood vessels. (A) The images of capillary tube reconstruction (with and without scaffold), and capillary tube distribution and diameter, together with statistically quantitative analysis of capillary tube (B) volume, (C) surface and (D) diameter. *: $p < 0.05$, **: $p < 0.01$

The time sequence of in vivo immune-neurovascular osseointegration was identified and exhibited via fluorescent staining of tissue sections around implanted scaffolds. At 1 w post-surgery, infiltrated macrophages displayed pro-inflammatory M1 phenotype for m-TC4, but switched anti-

inflammatory M2 state for 10%H_2O_2-Ca and 50%H_2O_2-M scaffolds, as verified by iNOS (M1 marker labelled as green) and CD206 (M2 marker labelled as red) fluorescent staining images along with quantitative analysis of their relative fluorescence intensity (Fig. 9A). At 2 w post-surgery, evident H-typed blood vessel identified by high expression levels of both CD31 and EMCN (namely $CD31^{high}$ $EMCN^{high}$) (*26, 36*) , neurogenesis and innervation (characterized by Nestin and Tubulin), as well as osteogenic differentiation (symbolled by Col-1 and OPN) were present around 10%H_2O_2-Ca, especially more prominent around 50%H_2O_2-M, rather than m-TC4 (Fig. 9A). Above-mentioned staining images (Fig. 9A) and their corresponding quantitative analysis (Fig. 9B-E) manifested that sequential healing reaction occurred, including inflammatory response, synchronized vascularization and neurogenesis, as well as subsequent osteogenesis, suggesting that inflammatory response initiated sequent neurovascular osseointegration. CD31 as an immunochemistry marker validated the angiogenesis. H-typed blood vessel identified in the skeletal system, a specific vessel subtype called $CD31^{high}EMCN^{high}$, actively propelled bone formation and encouraged angiogenic-osteogenic coupling during bone repair and reconstruction(*32*). Nestin, a specific neural marker, acted as an intermediate filament protein produced by neural stem cells, while tubulin as an early maturing neuronal marker, is involved in intracellular/axonal transport as well as structural maintenance (*35*). Col-1 as the major components of organic bone matrix, plays a crucial role in bone mechanical strength. Col I and OPN respectively as early and middle-stage indicators of osteogenic differentiation, powerfully supported osteogenesis. The fluorescent staining of tissue section around implanted scaffolds demonstrated the stimulative effect of functionally decorated coating with not only micro/nano gradient morphology but also sustainedly released multi bioactive ions on immune-neurovascular osseointegration. It uncovered immunoregulatory osteogenesis-angiogenesis and osteogenesis-innervation coupling relevance during bone healing.

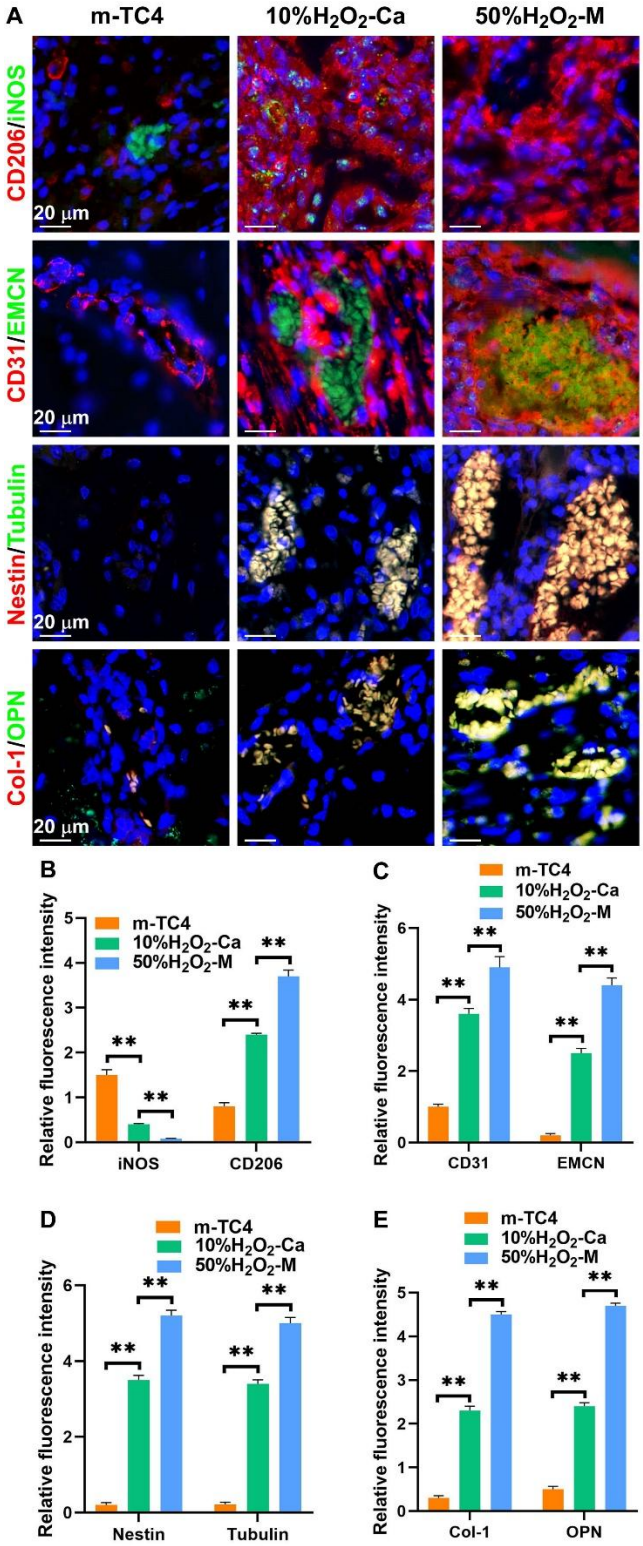


Fig. 9 Fluorescent staining of tissue sections around implanted scaffolds. (A) Fluorescent staining images of inflammatory markers (green-labeled iNOS for M1-typed macrophages and red-labeled CD206 for macrophages of M2 phenotype) at 1 w post-surgery, angiogenic markers (red-labeled CD31 and green-labeled EMCN), neural markers (red-labeled Nestin and green-labeled Tubulin), osteogenic markers (red-labeled Col-1 and green-labeled OPN) at 2 w post-surgery, and blue-labeled nuclei along with (B-E) their corresponding quantified statistics. *: $p < 0.05$, **: $p < 0.01$.

The newly formed bone within and around porous scaffolds were reconstructed according to micro-CT scanning data. Micro-CT reconstructed scaffolds (labeled as grey) and new bone within (labeled as yellow) and around (labeled as blue) porous scaffolds (Fig. 10A), along with their quantitative analysis (Fig. 10B-F, such as BV/TV, BS/BV, TbN, TbSp and TbTh) demonstrated new bone formation. It uncovered that 10%H_2O_2-Ca characterized with micro/nano gradient morphology obviously boosted osteogenesis inside and around porous scaffold in relative to m-TC4 with sole micro-scaled topography. It is worthy noting that 50%H_2O_2-M endowed with micro/nano gradient morphology as well as multifarious bioactive ion incorporation, exhibited significant acceleration for bone regeneration and reconstruction, indicating that synergistic action of both surface appearance and bioactive ion release. Fluorescence staining images of calcein and alizarin red visualized new bone at 4 and 8 w (Fig. 10G), and mineralization apposition rate (Fig. 10H) calculated from the gap between calcein and alizarin red fluorescence represented bone growth rate. Above-mentioned scaffolds contributed to new bone growth acceleration with the trend similar to that of micro-CT reconstructed new bone.

Moreover, freshly formed bone characterized by Van Geison staining (Fig. S2A) and their quantified percentage (Fig. S2B) disclosed that scarce bone emerged at the boundary of m-TC4, many new bones at the boundary of 10%H_2O_2-Ca, and abundant new bones at the boundary of 50%H_2O_2-M at 4 w post-surgery. However, little new bone regenerated at the boundary of m-TC4, and the facilitation of mineralized bone strengthened at the boundary of 50%H_2O_2-M in relative to 10%H_2O_2-Ca until 8 w post-surgery. To sum up, 50%H_2O_2-M expedited more new bone formation than 10%H_2O_2-Ca, and much more than m-TC4, providing a candidate staggery for surface functional decoration of 3D printed scaffolds.

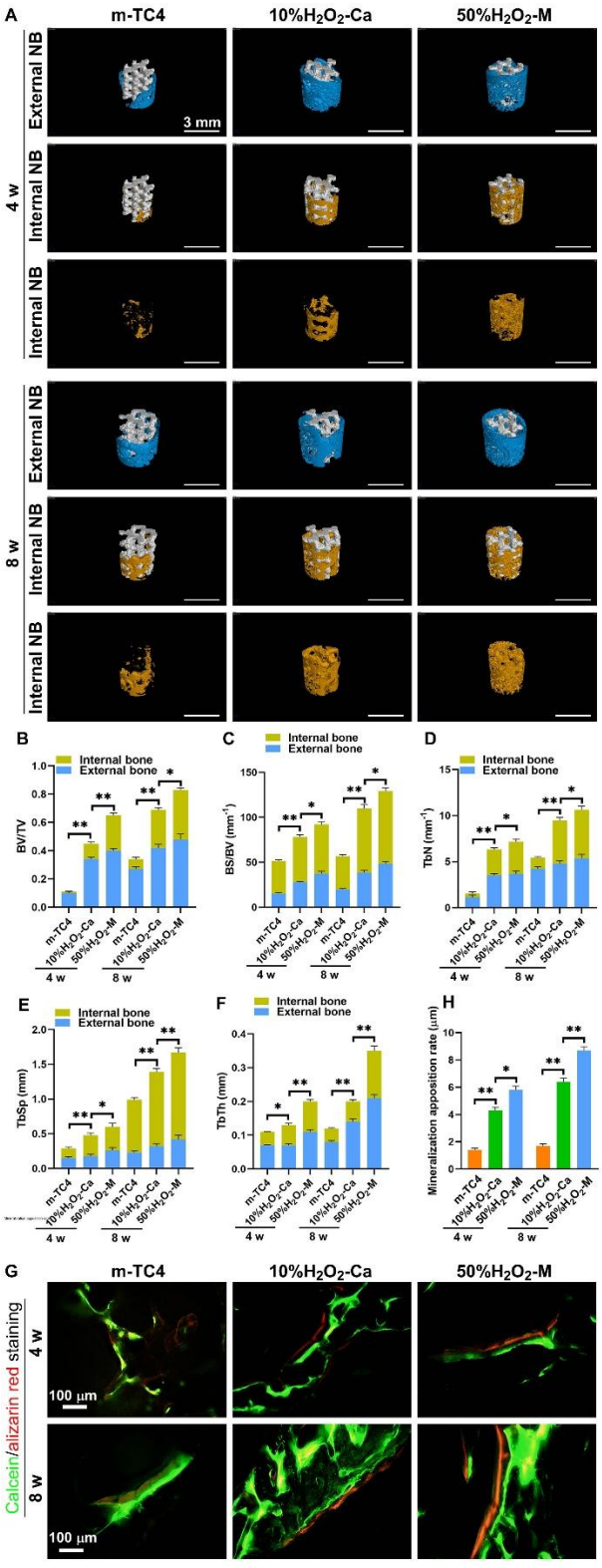


Fig. 10 New bone visualized by micro-CT and growth rate quantified by the gap between fluorescence green-labeled calcein and red-labeled alizarin red at 4 and 8 w post-surgery. (A) Micro-CT reconstructed scaffolds and new bone within and around (300 μm) porous scaffolds and (B-F) their corresponding quantifications. (G) Fluorescence staining images of calcein and alizarin red, along with (H) mineralization apposition rate calculated from the gap between calcein and alizarin red fluorescence.

Conclusion

Herein, bioactive ceramic coating of calcium titanate ($CaTiO_3$) nanogranule in-situ grown hydrothermally on titanium alloy scaffold surface with micro-scaled pit was established, and also trace other bioactive ions (such as Na^+, K^+, Mg^{2+} and Sr^{2+}) were incorporated into calcium titanate lattice during in-situ formation of this ceramic coating. Both micro/nano morphology and released bioactive ions synergistically regulated macrophages switch into anti-inflammatory phenotype (M2), accelerated in vitro and in vivo neurovascular bone regeneration via macrophage-secreted anti-inflammatory, pro-angiogenic, pro-neural and pro-osteogenic cytokines together with their crosstalk. Micro/nano gradient morphology along with dominant Ca ion and trace other bioactive ions, as one kind bioactive ceramic coating, were decorated on 3D printed titanium alloy scaffolds, providing a promising insight into functional modification of bone repair implants in specific clinical scenario. Currently, our biomaterial design and construction focus on smart self-regulated repair effect for bone defect, especially large segmental counterpart.

Experimental methods

Preparation of as-received and coated scaffolds

For as-received scaffolds (TC4), ϕ14×2 and ϕ3×5 mm sized porous titanium alloy scaffolds with diamond-structured pore (pore size of 600 um and porosity of 60%) from Wedo (Xian) Bio-Medical Technology Co., were fabricated by a selective laser melting (SLM) 3D printer (BLT-S310; Bright Laser Technologies Co., Ltd., China). For coated scaffolds (10%H_2O_2-Ca), acid-etched TC4 (m-TC4) scaffolds placed in Teflon-lined autoclaves containing the mixture solutions of 1 M NaOH, 1 M $CaCl_2$ and 10% H_2O_2 were in-situ hydrothermally synthesized at 180 °C for 4 h to obtain 10%H_2O_2-Ca scaffolds. For coated scaffolds (50%H_2O_2-M), acid-etched TC4 scaffolds placed in Teflon-lined autoclaves containing the mixture solutions of 1 M NaOH, 0.1 M KOH, 1 M $CaCl_2$, 0.1 M $SrCl_2$ and 0.01 M $MgCl_2$, as well as 50% H_2O_2 were in-situ hydrothermally synthesized at 180 °C for 4 h to obtain 50%H_2O_2-M scaffolds. All the abovementioned scaffolds were sterilized for the following biological evaluation.

Structural characterization

Low and high magnified surface morphology was captured using scanning electron microscope (SEM, SU6600, Japan), assisted with energy dispersive X-ray spectroscope (EDX, Japan) for element analysis. Phasic compositions of abovementioned coatings were examined by thin film X-

ray diffractometer (XRD, XPert Pro, Netherland). Nano-morphologies scratched from each kind of scaffolds were observed by a transmission electron microscope (TEM; JEOL-JEM 2100 F, Japan). Chemical species of scaffold surfaces were detected using an X-ray photoelectron spectroscopy (XPS, Thermo Scientific-ESCALAB 250Xi, US), calibrating with C1s peak at binding energy of 284.6 eV. Nano-scaled roughness values on coated scaffolds were tested by atomic force microscope (AFM, Bruker Dimension Icon, Germany). Each kind of coated scaffolds were respectively immersed in 10 mL phosphate buffer saline (PBS, K^+-free) solutions for 1, 3, 7, 14 and 30 d to collect extract liquid for concentration detection of released ion with inductively coupled plasma mass spectrometry (ICP-MS, Aglient-7800, US). The hydrophilicity on each kind of scaffold was detected using a contact angle device (DSA30, Kruss, Germany) for triplicate.

In vitro cellular assessment

Cell sources and cultures involved in this research were described in detail in supplementary information (SI).

Inflammatory response of macrophages on scaffolds: The abovementioned scaffolds (m-TC4,10%H_2O_2-Ca and 50%H_2O_2-M) were centrally placed in 24-well tissue culture plates respectively and then seeded with macrophages at a density of 2×10^4 cells per well, followed by incubation for 3 d. Polarized phenotypes of macrophages at 3 d were visualized with immunofluorescent staining. In brief, macrophages on scaffolds were rinsed with phosphate buffer saline (PBS) for three repetitions, immobilized using 4% paraformaldehyde and then pierced using 0.1 % Triton X-100, followed by blocking with 5 % bovine serum albumin (BSA). Thereafter, macrophages were cultured with rabbit anti-mouse primary antibody against inducible nitric oxide synthase (iNOS, Abcam, UK) at a dilution ratio of 1: 200 and sheep anti-mouse primary antibody against cluster of differentiation 206 (CD206, Abcam, UK) at a dilution ratio of 1:300 at 4 °C overnight, therewith using goat anti-rabbit IgG (Boster, China) and donkey anti-goat IgG (Boster, China) to respectively visualize iNOS and CD206 markers, along with DAPI (Servicebio, China) to stain cell nuclei. The immunofluorescent staining images were photographed by a laser scanning confocal microscope (LSCM; FV1200, Olympus, Japan) and their quantitative analysis of corresponding fluorescence intensity was conducted using Image Pro Plus 6.0 (Media Cybernetics, USA). Moreover, the scaffold-stimulated macrophage medium supernatant at 3 d was respectively collected to determine secretion levels of related cytokines by enzyme linked immunosorbent assay

(Elisa), such as tumor necrosis factor α (TNF-α), interleukin-10 (IL-10), vascular endothelial growth factor (VEGF), platelet-derived growth factor-BB (PDGF-BB), nerve growth factor (NGF) and bone morphogenetic protein 2 (BMP2).

Immunoregulatory angiogenesis and vascularization assay: Transwell invasion assay and scratch assay were applied to evaluate migration capability of HUVECs. For transwell invasion assay, HUVECs at a density of 2×10^4 cells per mL seeded in top chamber with 8 μm pore-sized permeable membrane were respectively incubated for 24 h with 3d-macrophage conditioned media (CM) of m-TC4,10%H_2O_2-Ca and 50%H_2O_2-M in the bottom chamber. Therewith, migrated HUVECs on the bottom of permeable membrane were fixed with 4 % paraformaldehyde for 20 min and stained using crystal violet staining solution (Beyotime, China). The photographs were captured by an inverted light microscope (CX21, Olympus, Japan) for the counting of invaded HUVECs with Image J soft. For scratch assay, HUVECs upon complete monolayer confluence of 6-well tissue culture plates were scratched perpendicular to plate surface using a 20 μL pipette. After respective culture with abovementioned CM for 0 and 24 h, cell migration images were acquired using an inverted light microscope (CX21, Olympus, Japan) for migration distance calculation with Image J software. Furthermore, capillary tube formation of HUVECs was observed and quantified. Briefly, HUVECs seeded at a density of 5×10^4 cells/well in 96-well tissue culture plate with 50 μL spread and gelatinized Matrigel, were respectively incubated with abovementioned CM for 12 h. Capillary tube network of HUVECs was visualized by an optical microscope (CX21, Olympus, Japan) for statistical quantitation of branch point number and capillary tube total capillary tube length using Image Pro Plus 6 software.

Immunoregulatory neurodifferentiation: Fluorescence staining of nestin and microtubule-associated protein 2 (MAP2) in NE-4C cells indicative of neural differentiation was conducted. Firstly, NE-4C cells seeded at a density of 2×10^4 cells per mL on cell slide centrally placed in 24-well tissue culture plates, were respectively incubated for 3 d with 3-d macrophage CM from m-TC4,10%H_2O_2-Ca and 50%H_2O_2-M scaffolds. Secondly, NE-4C cells were exerted fixation using 4 % paraformaldehyde, permeabilization with 0.1 % Triton X-100 and then blocking using 5 % BSA in turn. Whereafter, NE-4C cells were cultivated with rabbit anti-mouse primary antibody against nestin (Abcam, UK) at a dilution ratio of 1: 200 and sheep anti-mouse primary antibody against MAP2 (Abcam, UK) at a dilution ratio of 1: 300 at 4 °C overnight, followed with goat anti-rabbit

IgG (Boster, China) and donkey anti-sheep IgG (Boster, China) to respectively label nestin and MAP2 markers, along with DAPI (Servicebio, China) to stain cell nuclei. The fluorescent staining images were photographed by a laser scanning confocal microscope (LSCM; FV1200, Olympus, Japan) for statistical analysis of their corresponding fluorescence intensity with Image Pro Plus 6.0 (Media Cybernetics, USA).

Immunoregulatory osteogenic function: Alkaline phosphatase (ALP) staining and alizarin red staining were respectively applied to evaluate osteogenic function, including differentiation and mineralization. Briefly, MC3T3-E1 cells at a density of 2×10^4 cells per mL were seeded in 24-well tissue culture plate and respectively incubated for predetermined time with 3-d macrophage CM from m-TC4,10%H_2O_2-Ca and 50%H_2O_2-M scaffolds. MC3T3-E1 cells at 7 and 14 d were conducted for fixation with 4 % paraformaldehyde and respective staining with ALP staining kit (Abcam, UK) and alizarin red staining (ARS, Servicebio, China), followed by observation using an inverted light microscope (DM1000, Leica, Germany).

RNA Sequencing (RNA-seq) and Data Analysis: After 3-d respective incubation of macrophages on m-TC4 and 50%H_2O_2-M scaffolds, corresponding macrophages were collected from the scaffolds, followed by total RNA extraction using TRIzol reagent (Invitrogen, Carlsbad, CA, USA). Thereafter, mRNA enrichment, fragmentation, reverse transcription, library construction, HiSeq X Ten along with data analyses were conducted sequentially by Genergy Biotechnology Co. Ltd. (Shanghai, China). The thresholds of differentially expressed transcripts (DETs) were $p < 0.05$ and an absolute fold change $\geqslant 2$. DETs for functional and signaling pathway enrichment analyses were executed with Gene Oncology (GO) and Kyoto Encyclopedia of Genes and Genomes (KEGG) databases. GSEA was used to analyze the differences between m-TC4 and 50%H_2O_2-M groups in a pre-defined gene set.

In vivo animal evaluation

Immunoregulatory, angiogenic, neuralized and osteogenic functions stimulated by scaffolds *in vivo*: The animal experiment got approval from Institutional Animal Care Committee and Research Ethics Committee of Air Force Medical University (Ethics number: IACUC-20230659). Forty-eight Sprague Dawley (SD) rats (male, 10-week-old, weighing ~250 g) were randomly divided in three groups, with sixteen rats each group. The rats were intraperitoneally injected with sodium pentobarbital at a dose of 10 mg/100g for anesthesia. Standardized femoral condyle defects (ϕ3×5

mm) were created and then implanted with scaffolds in both hind limb femoral condyles of a rat (one scaffold per femoral condyle), followed by suture layer by layer. The rats received perioperative antibiotics (50 kU/kg penicillin) by intramuscular injection and postoperative medical care. Four rats in each group post-surgery were sacrificed with overdose an aesthesia at 1, 2, 4 and 6 w respectively.

Femoral condyles containing scaffolds were collected for new bone and angiogenesis detection with Micro-computed tomography (Micro-CT, AX-2000, Always Imaging, China) at source voltage of 130 kV, beam current of 100 μA and scanning resolution of 8.68 μm. 3D reconstruction and statistical quantification of bone volume percentage (BV/TV), specific surface area (BS/BV), trabecular number (TbN), trabecular septum (TbSp) and trabecular thickness (TbTh), were executed with AYRecon Auto V3.5 software and VG Studio MAX 3.5, respectively.

For histological immunofluorescence staining, scaffold-removed femoral condyles were fixed with 4 % paraformaldehyde, decalcified in 10 % EDTA solution, dehydrated in gradient ethanol and embedded into paraffin for obtaining 5 μm thin sections using a cutting-unit (Leica, Germany). Thereafter, the decalcified sections were carried out iNOS/CD206, CD31/endomucin (EMCN), Nestin/Tubulin, Col-1/OPN and nuclei fluorescence staining respectively with corresponding rabbit anti-mouse and sheep anti-mouse primaries at a dilution ratio of 1: 200. The fluorescence staining images were photographed by a laser scanning confocal microscopy (LSCM, FV1000, Olympus, Japan), followed by quantified analysis using Image J software.

For undecalcified tissue analysis, the scaffold-containing femoral condyle specimens were fixed with 4 % paraformaldehyde, sequentially dehydrated using 70%, 80%, and 90% n-butyl alcohol, absolute ethanol, and xylene for 2 h in each solution. Whereafter, the specimens were embedded and cut into ≈10 mm thin sections. And then sections were polished and stained with VG for imaging using a microscope (CX21; Olympus, Japan).

For fluorescent observation of newly formed bone, calcein and alizarin red staining were used to respectively visualize new bone tissue at 4 and 8 weeks. Calcein solution (5 mg/kg) at 10 days and alizarin red solution (75 mg/kg) at 3 days before sacrifice respectively were injected intramuscularly. Subsequently, the scaffold-containing femoral condyle specimens were fixed, dehydrated, embedded and cut into ≈150 mm thin sections, as above-mentioned description. the fluorescence staining images were captured by fluorescence microscope. The growth rate of new

bone, characterized by the bone mineral deposition rate (MAR), was calculated based on the distance between calcein and alizarin red staining lines, according to fluorescence images of calcein and alizarin red staining.

Statistical analysis: All experiments were performed at least 3 independent replications. Quantitative data performed using SPSS 19.0 software were expressed as mean ± standard deviation (SD). Significant differences between groups were determined with one-way analysis of variance (ANOVA) and Student-Newman-Keuls (SNK) post hoc test. The thresholds of difference levels were of *: $p< 0.05$, **: $p< 0.01$ and ***: $p<0.001$.

Acknowledgements

Dongmei Yu, Zhen Tang and Tonglei Yang contributed equally to this work. This work was financially supported by grants from the National Key Research and Development Program of China (Grant No. 2023YFC2412600), Central guidance for local scientific and technological development special project (2024FRD05100) and National Natural Science Foundation of China (Grant Nos. 82372124, 82402479, and 82402771). The authors also appreciate the support from the Incubation Project of Army's Medical Technology Youth Cultivation Program of China (17QNP021), the Everest Program of Air Force Medical University (2020ZFC002) and the Phoenix Introduction Plan Talent Startover Project of Tangdu Hospital, Air Force Medical University (2022YFJH004). The authors appreciate the Department of Product Research & Development, Wedo (Xian) Bio-Medical Technology Co., Ltd for providing pristine 3D printed scaffolds and Centre for Advancing Materials Performance from the Nanoscale (CAMP-Nano) of Xi'an Jiaotong University for some material characterization test.

Reference

1. H. Shao, K. Wen, R. Liu, N. Ding, Y. Gong, Y. Zhuang, Y. He, 3D Printing of Bioceramic Multifunctional Scaffolds for Bone Tissue Engineering. *Advanced Functional Materials*, e09039 (2025).
2. X. Yuan, W. Zhu, Z. Yang, N. He, F. Chen, X. Han, K. Zhou, Recent Advances in 3D Printing of Smart Scaffolds for Bone Tissue Engineering and Regeneration. *Advanced Materials* **36**, (2024).
3. W. Abd-Elaziem, M. A. Darwish, A. Hamada, W. M. Daoush, Titanium-Based alloys and composites for orthopedic implants Applications: A comprehensive review. *Materials & Design*

241, (2024).

4. D. Yu, S. Wu, T. Zhao, Y. Zhang, L. Yao, Z. Zheng, T. Li, H. Wu, N. Wang, X. Li, C. Liu, Z. Guo, Nanograin-enhanced surface-layer strengthening of 3D printed intervertebral cage induced by sandblasting. *Biomedical Materials* **20**, (2025).
5. M. Sun, C. Xu, R. Wu, Q. Yang, X. Ding, N. Zhao, W. Geng, Y. Sun, S. Duan, F. J. Xu, Surface-Engineered Orthopedic Implant to Break the Antimicrobial-Osteogenic Paradox at Biointerfaces in the "Race for the Surface". *Advanced Materials* **37**, (2025).
6. C. H. Sung, T. Hao, H. Fang, A. T. Nguyen, V. Perricone, H. Yu, W. Huang, E. Sarmiento, A. F. D. Ornelas, D. Lublin, R. Wehling, S. Farajollahi, A. Arakaki, D. Nepal, N. P. Lord, D. Kisailus, Biological and Biologically Inspired Functional Nanostructures: Insights into Structural, Optical, Thermal, and Sensing Applications. *Advanced Materials*, (2025).
7. X. He, Z. Han, Y. Ruan, Z. Wang, B. Liao, X. Li, J. Tan, X. Han, J. Shen, D. Bai, Smart responsive biomaterials for spatiotemporal modulation of functional tissue repair. *Materials Today Bio* **33**, (2025).
8. Y. C. Zhiguo Bi, Xiaotong Shi, Jintian Chen, Dongsong Li, Peibiao Zhang, Jianguo Liu, Macrophage-mediated immunomodulation in biomaterial-assisted bone repair: Molecular insights and therapeutic prospects. *Chemical Engineering Journal* **488**, (2024).
9. X. Zhao, M. Yao, Y. Wang, C. Feng, Y. Yang, L. Tian, C. Bao, X. Li, X. Zhu, X. Zhang, Neuroregulation during Bone Formation and Regeneration: Mechanisms and Strategies. *ACS Appl Mater Interfaces* **17**, 7223-7250 (2025).
10. J. L. Yanan Zhao, Liangcong Hu, Xiaokang Yao, Rong Tu, Takashi Goto, Lianmeng Zhang, Xiaopei Wu, Guohui Liu, Honglian Dai, Novel "hot spring"-mimetic scaffolds for sequential neurovascular network reconstruction and osteoporosis reversion. *Biomaterials* **320**, 123191 (2025).
11. X.-L. Li, Y.-Q. Zhao, L. Miao, Y.-X. An, F. Wu, J.-Y. Han, J.-Y. Han, F. R. Tay, Z. Mu, Y. Jiao, J. Wang, Strategies for promoting neurovascularization in bone regeneration. *Military Medical Research* **12**, (2025).
12. T. Xu, L. Gan, W. Chen, D. Zheng, H. Li, S. Deng, D. Qian, T. Gu, Q. Lian, G. Shen, Q. An, W. Li, Z. Zhang, G. Y. Yang, H. Ruan, W. Cui, Y. Tang, Bridging immune-neurovascular crosstalk via the immunomodulatory microspheres for promoting neural repair. *Bioact Mater* **44**, 558-571 (2025).
13. Y. Zhao, J. Liu, L. Hu, X. Yao, R. Tu, T. Goto, L. Zhang, X. Wu, G. Liu, H. Dai, Novel "hot spring"-mimetic scaffolds for sequential neurovascular network reconstruction and osteoporosis reversion. *Biomaterials* **320**, (2025).
14. S. Li, Y. Cui, H. Liu, Y. Tian, G. Wang, Y. Fan, J. Wang, D. Wu, Y. Wang, Application of bioactive metal ions in the treatment of bone defects. *J Mater Chem B* **10**, 9369-9388 (2022).
15. S. Liu, Z. Lin, W. Qiao, B. Chen, J. Shen, Cross-talk between biometal ions and immune cells for bone repair. *Engineered Regeneration* **5**, 375-408 (2024).
16. M. Hao, D. Zhang, W. Wang, Z. Wei, J. Duan, J. He, X. Kong, Y. Sang, S. Feng, H. Liu, HAp Thermosensitive Nanohydrogel Cavities Act as Brood Pouches to Incubate and Control-Release NSCs for Rapid Spinal Cord Injury Therapy. *Advanced Functional Materials* **32**, (2022).
17. D. Yu, Z. Tang, S. Bao, S. Guo, C. Chen, Q. Wu, M. Wang, Z. Zheng, P. Cao, B. Xu, H. Wu, N. Wang, H. Huang, C. Liu, X. Li, Z. Guo, Immunoregulatory Neuro-Vascularized Osseointegration Driven by Different Nano-Morphological CaTiO3 Bioactive Coatings on

Porous Titanium Alloy Scaffolds. *Advanced Healthcare Materials* **14**, (2025).

18. P. Zhou, T. Liu, W. Liu, L. Sun, H. Kang, K. Liu, P. Luo, Y. Wang, L. Luo, H. Dai, An Antibacterial Bionic Periosteum with Angiogenesis-Neurogenesis Coupling Effect for Bone Regeneration. *ACS Appl Mater Interfaces* **16**, 21084-21097 (2024).
19. D. Yu, B. Li, M. Yu, S. Guo, Z. Guo, Y. Han, Cubic multi-ions-doped Na(2)TiO(3) nanorod-like coatings: Structure-stable, highly efficient platform for ions-exchanged release to immunomodulatory promotion on vascularized bone apposition. *Bioact Mater* **18**, 72-90 (2022).
20. D. Yu, Z. Tang, S. Bao, S. Guo, C. Chen, Q. Wu, M. Wang, Z. Zheng, P. Cao, B. Xu, H. Wu, N. Wang, H. Huang, C. Liu, X. Li, Z. Guo, Immunoregulatory Neuro-Vascularized Osseointegration Driven by Different Nano-Morphological CaTiO(3) Bioactive Coatings on Porous Titanium Alloy Scaffolds. *Adv Healthc Mater*, e2404647 (2025).
21. H.-C. Hsu, T.-Y. Shih, S.-C. Wu, W.-F. Ho, Preparation of titania nanowires/calcium titanate hybrid structure on titanium surface through hydrothermal treatment and using oyster shell as calcium source. *Surface and Coatings Technology* **481**, (2024).
22. J. Li, H. Wu, R. Zhong, Y. Wang, S. Ye, H. Zhao, K. Yan, Y. Zhu, Z. Hu, W. Xie, T. Zhang, Quenching-induced oxygen vacancy engineering boosts photocatalytic activities of CaTiO3. *Applied Surface Science* **670**, (2024).
23. S. Guo, D. Yu, C. Zhao, W. Liu, M. Wang, B. Hu, B. Xu, L. Ren, S. Zhang, J. Ma, X. Qu, C. Li, Z. Zhao, N. Jiang, Z. Wu, X. Li, C. Tang, Z. Guo, E. Luo, Micro-nano scale Mg-containing SrTiO3 nanofilm spacially sustained release platform promotes bone regeneration by stereoscopic repair of immune-vasculature network. *Materials & Design* **257**, (2025).
24. C. Zhao, X. Zhang, C. Li, C. Liu, Y. Zhou, Z. Hu, D. Sun, H. Zhai, L. Wang, Alkalized oxygen deficient engineering of strontium titanate: Effective carrier extraction and electronic structure regulation. *Journal of Alloys and Compounds* **1035**, (2025).
25. D. Yu, S. Guo, M. Yu, W. Liu, X. Li, D. Chen, B. Li, Z. Guo, Y. Han, Immunomodulation and osseointegration activities of Na2TiO3 nanorods-arrayed coatings doped with different Sr content. *Bioactive Materials* **10**, 323-334 (2022).
26. D. Yu, B. Li, M. Yu, S. Guo, Z. Guo, Y. Han, Cubic multi-ions-doped Na2TiO3 nanorod-like coatings: Structure-stable, highly efficient platform for ions-exchanged release to immunomodulatory promotion on vascularized bone apposition. *Bioactive Materials* **18**, 72-90 (2022).
27. N. A. Morozov, D. S. Ershov, O. Y. Sinel'shchikova, N. V. Besprozvannykh, S. V. Mjakin, E. Y. Brazovskaya, O. L. Galankina, A. V. Koroleva, Effect of magnesium additive on acid-base properties and photocatalytic activity of nanostructured potassium titanate. *Applied Surface Science* **644**, (2024).
28. C. S. Wu, C. Y. Chen, C. H. Yang, Y. P. Hsu, C. H. Yu, Y. H. Chen, S. K. Chen, The alterations of molecular repertoire of the RANKL-induced osteoclastogenesis in the M1 macrophage-derived inflammatory milieu. *Sci Rep* **15**, 16137 (2025).
29. L. Chen, J. Zhu, N. Ge, Y. Liu, Z. Yan, G. Liu, Y. Li, Y. Wang, G. Wu, T. Qiu, H. Dai, J. Han, C. Guo, A biodegradable magnesium alloy promotes subperiosteal osteogenesis via interleukin-10-dependent macrophage immunomodulation. *Biomaterials* **318**, 122992 (2025).
30. F. Dai, J. Zhang, F. Chen, X. Chen, C. J. Lee, H. Liang, L. Zhao, H. Tan, A Multi-Responsive Hydrogel Combined With Mild Heat Stimulation Promotes Diabetic Wound Healing by Regulating Inflammatory and Enhancing Angiogenesis. *Adv Sci (Weinh)* **11**, e2408783 (2024).

31. Q. W. Wenjing Liu, Haiyun Luo, Bichong Luo, Fujian Zhao, Yiyuan Kang, Yanli Zhang, Longquan Shao, Nanographene Oxide Promotes Angiogenesis by Regulating Osteoclast Differentiation and Platelet-Derived Growth Factor Secretion. *ACS Nano* **18**, 22390–22403 (2024).
32. Z. Shen, W. Dong, Z. Chen, G. Chen, Y. Zhang, Z. Li, H. Lin, H. Chen, M. Huang, Y. Guo, Z. Jiang, Total flavonoids of Rhizoma Drynariae enhances CD31hiEmcnhi vessel formation and subsequent bone regeneration in rat models of distraction osteogenesis by activating PDGF-BB/VEGF/RUNX2/OSX signaling axis. *International Journal of Molecular Medicine* **50**, (2022).
33. Z. Li, C. A. Meyers, L. Chang, S. Lee, Z. Li, R. Tomlinson, A. Hoke, T. L. Clemens, A. W. James, Fracture repair requires TrkA signaling by skeletal sensory nerves. *J Clin Invest* **129**, 5137-5150 (2019).
34. H. Shen, J. Shi, Y. Zhi, X. Yang, Y. Yuan, J. Si, S. G. F. Shen, Improved BMP2-CPC-stimulated osteogenesis in vitro and in vivo via modulation of macrophage polarization. *Mater Sci Eng C Mater Biol Appl* **118**, 111471 (2021).
35. Y. Xu, C. Xu, L. He, J. Zhou, T. Chen, L. Ouyang, X. Guo, Y. Qu, Z. Luo, D. Duan, Stratified-structural hydrogel incorporated with magnesium-ion-modified black phosphorus nanosheets for promoting neuro-vascularized bone regeneration. *Bioact Mater* **16**, 271-284 (2022).
36. H. Quan, C. Ren, H. Xie, Z. He, H. Ding, J. Li, T. Li, F. Wang, S. Dong, H. Jiang, An injectable hydrogel loaded with miRNA nanocarriers promotes vessel-associated osteoclast (VAO)-mediated angiogenesis and bone regeneration in osteonecrosis of the rat femoral head. *Biomaterials* **320**, 123252 (2025).

Supplementary Files

This is a list of supplementary files associated with this preprint. Click to download.

- ManuscriptSI.docx